Superresolution Three-Dimensional Images of Fluorescence in Cells with Minimal Light Exposure

Walter A. Carrington,* Ronald M. Lynch, Edwin D. W. Moore, Gerrit Isenberg, Kevin E. Fogarty, Fredric S. Fay

Fluorescent probes offer insight into the highly localized and rapid molecular events that underlie cell function. However, methods are required that can efficiently transform the limited signals from such probes into high-resolution images. An algorithm has now been developed that produces highly accurate images of fluorescent probe distribution inside cells with minimal light exposure and a conventional light microscope. This method provides resolution nearly four times greater than that currently available from any fluorescence microscope and was used to study several biological problems.

Conventional light microscopes equipped with cooled charge-coupled device (CCD) cameras of high quantum efficiency have the sensitivity to acquire multiple images of faint fluorescently labeled living cells with minimal photodamage or photobleaching (*1*). Images at several planes of focus (optical sections) provide three-dimensional information; however, each optical section of a three-dimensional fluorescent cell has many details obscured by blurred light from parts of the cell that are out of focus. Several microscopes have been developed that reduce out-of-focus haze or increase resolution, but their application to dynamic cellular processes has been limited by photodamage and photobleaching (*2*), slow data acquisition (*2*, *3*), or the requirement that the specimen be very thin (*4*). Images with enhanced resolution and reduced out-of-focus haze have also been produced by applying various image restoration methods to a series of images taken through-focus with a standard fluorescence microscope (*5*–*11*). These methods require that images be acquired with small pixels, necessitating high light exposures to achieve an adequate signal-to-noise ratio. Furthermore, these methods have not been applied to the study of dynamic processes in living cells because images must be acquired by focusing at planes regularly and closely spaced throughout the cell, which results in long data acquisition times, photobleaching, and photodamage. An algorithmic framework was therefore developed to produce high-resolution images from fewer image planes.

To make maximal use of all the detected photons from fluorescent probes in a cell and thus minimize light exposure, we modeled the imaging process as consisting of a finite amount of data (discrete data) formed from a continuous object. The camera has only a finite number of pixels and only a finite number of optical sections can be acquired, so the measured data are discrete. However, the cell is not composed of pixels and hence our model considered the cell as a continuous object. Thus, our formulation did not require the exact one-to-one correspondence between voxels of data and voxels of cell that is often assumed in image processing, nor did it require that the image be sampled on a regular grid of equally spaced pixels or uniformly spaced optical sections. The discrete-data and continuous-object model of the imaging process provided an algorithmic framework with an important practical advantage for biological experiments—its data sampling requirements were flexible and thus data acquisition protocols could be determined by the needs of the biological experiment rather than by the needs of a rigid algorithm. This approach also provided a unified way to deal with problems associated with processing of images of fluorescently labeled cells.

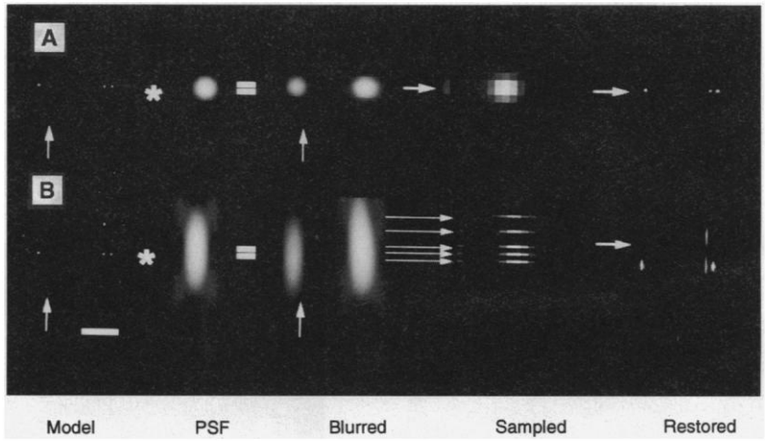

Fig. 1. Simulation of the discrete-data, continuous-object model of the imaging process in a conventional fluorescence microscope. (**A**) An *xy* view of the imaging process (*y* is vertical direction). (**B**) An *xz* view of the imaging process (*z* is vertical direction). Model: The computer model consists of four point sources of equal brightness at coordinates (−0.1, 0, 0), (4.1, 0, 0), (4.2, 0, 0), and (4.1, 0, 0.4) micrometers; the vertical arrows indicate the left edge of the camera at $x = 0$, with the first point thus outside the camera field of view. The continuous nature of the model is approximated here by the use of very small voxels (25 nm by 25 nm by 25 nm). PSF: The three-dimensional optical blurring of the microscope is characterized by its continuous point spread function (PSF), which is also approximated here by 25 nm by 25 nm by 25 nm voxels. The PSF used is calculated for an ideal objective with a numerical aperture of 1.4 in a conventional microscope (*17*). The PSF continues indefinitely in the *z* direction. Blurred: The continuous three-dimensional distribution of light from the model object is calculated by the convolution (asterisk) of the model with the PSF. The blurred light from the sources continues indefinitely in the *z* direction and spreads across the edge of the camera. Sampled: The three-dimensional continuous light distribution is sampled by acquiring optically sectioned images in a CCD camera. The left-most point source is outside the left edge of the camera and contributes light to each plane of the optically sectioned camera images, especially to out-of-focus planes. The camera is divided into a regular grid of square photosensitive detectors, 100 nm by 100 nm pixels. Sampling of the continuous light distribution in the *z* direction (optical sectioning) consisted of images at focal planes at $z = 0.0$, 0.1, 0.2, 0.4, and 0.6 μm. Restored: On the right are the images generated by restoring the data shown to a restoration grid with 25 nm by 25 nm by 25 nm subvoxels. The positions of the maxima of the restored point sources gave the exact relative positions except for the last point, which was off by 25 nm in *z*. The integrated intensities of the points had errors of 0.38, 2.48, 4.9, and 0.68%, respectively. $\alpha = 2 \times 10^{-11}$ and 1200 iterations were used. In all images, zero intensity was black and the brightest pixel was white. Scale bar (bottom left), 500 nm.

W. A. Carrington, K. E. Fogarty, F. S. Fay, Biomedical Imaging Group, Program in Molecular Medicine, University of Massachusetts Medical School, Worcester, MA 01605, USA.
R. M. Lynch, Department of Physiology, University of Arizona, Tucson, AZ 85274, USA.
E. D. W. Moore, Department of Physiology, University of British Columbia, Vancouver, British Columbia V6T 1Z3, Canada.
G. Isenberg, Department of Physiology, Martin-Luther-Universität, Halle-Wittenberg, Medizinische Fakultät, Julius-Bernstein-Institut für Physiologie, Magedeburger Strasse 6, 06097 Halle, Germany.

*To whom correspondence should be addressed.

The algorithm was based on the following formulation of the imaging process. At each optical section, each pixel collects light from a considerable volume of the cell, and the sensitivity of the pixel to a point source depends on the location of the source. Thus, the light collected by pixel i is a weighted sum of the fluorescence in the volume of the entire sample:

$$g_i = \int\int\int_V k_i(x,y,z)f(x,y,z)dxdydz \quad (1)$$

where $f(x,y,z)$ is the fluorescent dye density at (x,y,z); $k_i(x,y,z)$ is the response of a detector (camera pixel) to light from a point source located at (x,y,z) transmitted through the optics with the pixel focused onto the point (x_i,y_i,z_i); V is a volume containing the fluorescent specimen; $i = 1, 2, 3, \ldots, N$; and N is the number of sampled voxels of the image. The actual measurement $\tilde{g}_i$ will contain noise. The sampling points (x_i,y_i,z_i) may be distributed arbitrarily, but with a CCD camera the sampling in xy is fixed by the camera geometry and only the plane of focus can be controlled.

The determination of the dye density $f(x,y,z)$ from (1) is an ill-posed problem (*8*, *9*, *12–14*), to which we applied an L^2 regularization incorporating the powerful constraint that the dye density must be nonnegative. Thus, we estimate the dye density as the nonnegative function, $f(x,y,z) \geq 0$, that minimizes (*15*)

$$\Phi(f) = \sum_{i=1}^{N} | \tilde{g}_i - \int\int\int_V k_i(x,y,z)f(x,y,z)dxdydz|^2 + \alpha \int\int\int_V |f(x,y,z)|^2 dxdydz \quad (2)$$

The parameter α balances between the need to fit the data (first term) and the need to stabilize the estimate (second term); it is set by inspection, with a single value usually being adequate for all the images in a given experiment, or it may be set so that the first term equals the noise variance (*12–14*).

This framework was applied to a computer simulation of a three-dimensional image of a model specimen (Fig. 1). Light from the specimen originated from outside the field of view of the camera and light from objects inside the field of view blurred beyond the edges of the camera and beyond the z extent of the optical sections. The truncation of the data at the camera edges and in the z direction can cause artifacts at the edges of the images that standard algorithms deal with by rolling the data off to zero at the edges (apodization) or by circular interpolation (6), which artificially introduce errors in the data. Our approach eliminated these edge effects by restoring the dye density to a larger volume than the data without further assumptions on the light distribution outside the sampled volume. This approach also allowed us to perform the restoration on a finer grid than the sampling of the data. With 100-nm camera pixels, we restored the data to a 25-nm grid and resolved two point sources separated by only 100 nm in x and two point sources separated by 400 nm in z (Fig. 1). The light from each of these three point objects was assigned by the algorithm to a volume of <23% of the volume of a single voxel in the original sampled images. Whereas similar results could perhaps have been obtained with 25-nm voxel data, the light exposure to the specimen and the data acquisition time would be greatly increased. Use of the nonnegativity constraint enabled extension of the band limit (superresolution) of the restored images to considerably beyond the optical band limit of the microscope (*16*).

The extended resolution available from the algorithm requires a finely sampled point spread function (PSF) for the microscope. However, measuring a PSF with small fluorescent beads at such high magnification is difficult because the images are very faint, especially when out of focus. Although progress has been made in calculating ideal PSFs (*17*, *18*), they are

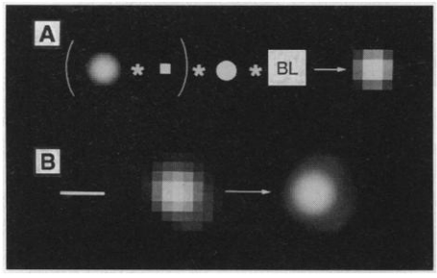

Fig. 2. Determination of a high-resolution three-dimensional PSF from the image of a 189-nm fluorescent bead. (**A**) Simulation of process of imaging a bead. The bead image is formed by convolving (from left to right) the continuous optical PSF with the square 112-nm camera pixel, the 189-nm bead, and a band-limiting function, BL, then sampling to get 112-nm pixels. (**B**) Measured bead and calculated PSF. (**Left**) One optical section image of a 189-nm bead with 112-nm pixels and 100-nm Δz taken with a Nikon 60× oil immersion lens with a numerical aperture of 1.4. (**Right**) A PSF with 28-nm (112 nm/4) pixels in xy and 50-nm steps in Δz calculated by applying our deconvolution algorithm to the bead image (*26*). All images shown are the in-focus plane of a three-dimensional image. Scale bar, 0.5 μm.

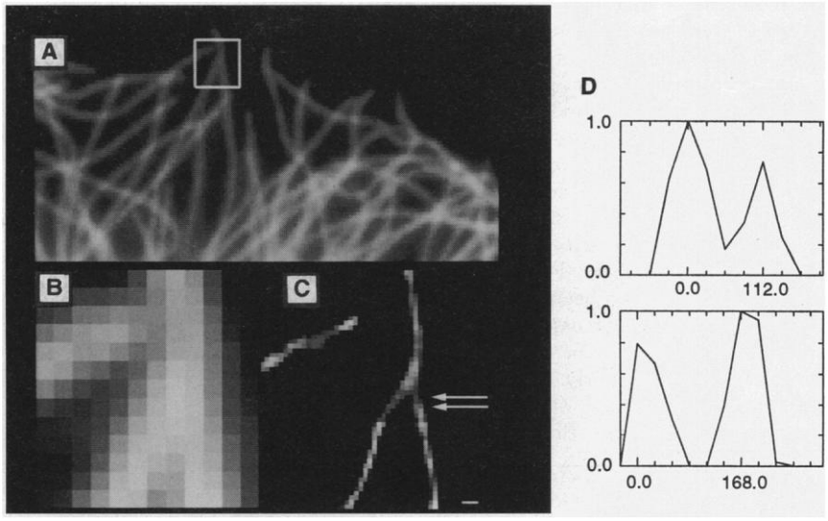

Fig. 3. High-resolution image of fluorescently labeled microtubules in an NRK-1 (normal rat kidney) cell obtained by restoring images to subpixel resolution. Images were collected with a Nikon 60× planapo objective with a numerical aperture of 1.4 at 0.1-μm intervals through focus with 112 nm per pixel. (**A**) View of the unrestored cell as a projection of a 0.35-μm-thick section. A region of the cell (boxed) contains a pair of microtubules that are oriented toward each other at a shallow angle. (**B**) Boxed region of the unrestored cell magnified. (**C**) Boxed region magnified after restoration to subpixel (28-nm) resolution also shown as a projection of a 0.35-μm-thick section. Scale bar (lower right), 100 nm. (**D**) The intensity along the rows of pixels in the restored cell at the positions indicated by the white arrows in (C) (*27*). In each image, zero intensity was black and the brightest pixel was white. $\alpha = 10^{-8}$ and 2000 iterations were used.

still inadequate for incorporating the aberrations in a particular microscope. Our deconvolution method was used to calculate this finely sampled PSF from a more coarsely sampled image of a 189-nm bead (Fig. 2).

We also tested resolution on a biological sample—a fixed cell with fluorescently labeled microtubules. We determined the smallest resolvable distance between two microtubules that appeared to be oriented toward each other at a shallow angle. The unrestored data (Fig. 3, A and B) with voxel size 112 nm by 112 nm by 100 nm was restored with subvoxels of 28 nm by 28 nm by 50 nm (Fig. 3C). The microtubules were resolved when only 112 nm apart with an 80% decrease in intensity between the two peaks (Fig. 3D). We calculated that to achieve the same dip in intensity, a wide-field microscope without restoration would require a 588-nm separation of two point sources and an ideal confocal microscope with the same optics would require a 420-nm separation. Thus, this image restoration to subpixel resolution extended the resolution of the light microscope nearly fourfold. The light from each stained microtubule was confined to three 28-nm subpixels in the restored image in the x direction, which was only slightly greater than the nearly 50-nm diameter of a microtubule (25 nm) plus a shell of primary and secondary antibodies (2×12 nm).

We also applied the image restoration algorithm to another more complex three-dimensional biological specimen, a fixed isolated smooth muscle cell in which the dihydropyridine and ryanodine receptors were labeled with specific fluorescently tagged antibodies (Fig. 4). Whereas the unrestored images provided only vague indications of the locations of these proteins, the images that had been restored to subpixel resolution indicated their nearly identical patterns of distribution (Fig. 4, D and H). This observation suggests that, in smooth muscle, Ca^{2+}-induced Ca^{2+} release, which has a relatively low sensitivity to Ca^{2+} concentration (*19*), may nevertheless be triggered by brief, small inward currents (*20*) that produce small changes in Ca^{2+} concentration in the bulk cytosol but large changes near the dihydropyridine influx channel.

The ability to provide quantitative accuracy (*21*) while minimizing light exposure and data acquisition time by the use of a small number of planes allows experiments with fluorescent analog probes to be performed in living cells that are not possible with alternative approaches. The number of photons available from each probe is limited by photobleaching, and the number of fluorescent analogs that can

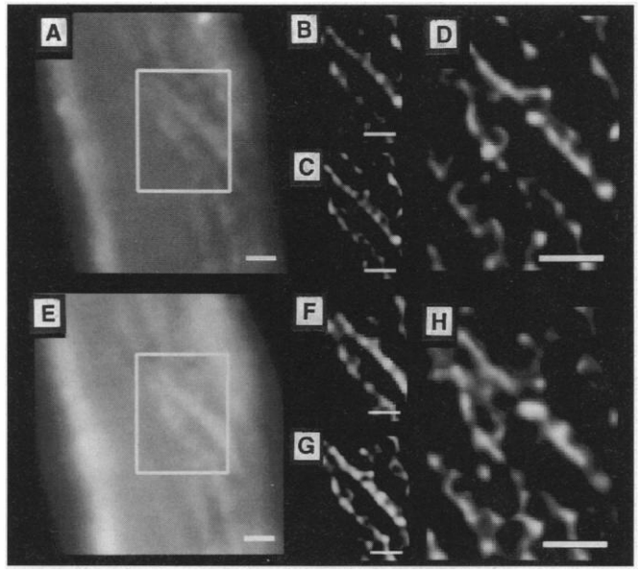

Fig. 4. High-resolution images of the distribution of ryanodine receptors (**A** to **D**) and dihydropyridine receptors (**E** to **H**) in a single enzymatically isolated smooth muscle cell from guinea pig bladder. (A and E) One optical section of the original data. (B and F) One plane of a conventional restoration of the boxed region with voxels in the restoration equal in size to those in the data (93 nm by 93 nm by 250 nm). (C and G) The boxed region restored by subpixel restoration with a voxel size of 46.5 by 46.5 by 125 nm; that is, interpolated by a factor of 2 in x, y, and z. (D and H) Volume rendering of subpixel restoration of boxed region, consisting of 10 planes (1.25 μm) rendered with a back-to-front opacity weighting (proportional to intensity) with the use of a reflectance lighting model in which the direction of reflection is the intensity gradient at each voxel. The antibodies to the ryanodine receptor and the dihydropyridine receptor were detected with secondary antibodies labeled with rhodamine and fluorescein, respectively (*11*). All scale bars, 1 μm. (B and F) $\alpha = 3 \times 10^{-5}$ and 120 iterations were used. (C, D, G, and H) $\alpha = 3 \times 10^{-6}$ and 600 iterations were used. In all images except (D) and (H), zero intensity was black and the brightest pixel was white.

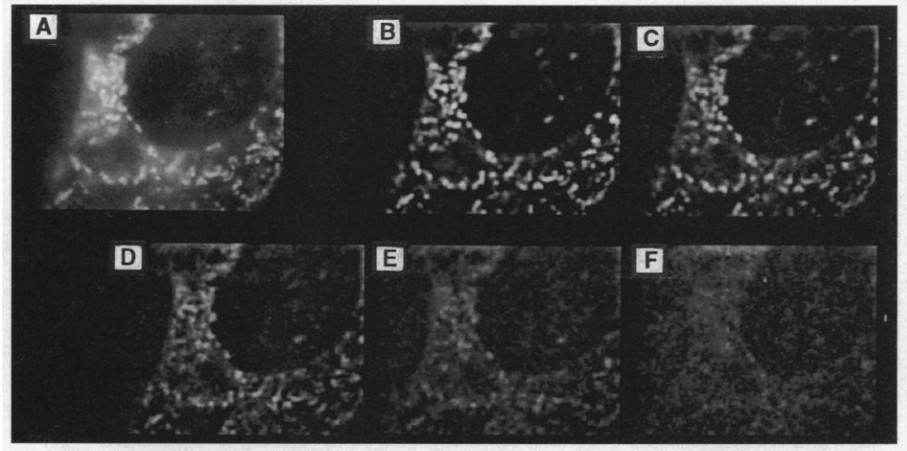

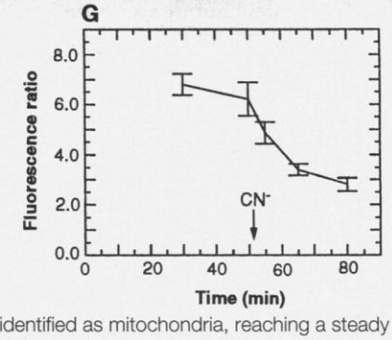

Fig. 5. Changes in the distribution of hexokinase in a single A7R5 cultured smooth muscle cell after inhibition of oxidative metabolism. The cell was injected with fluorescently labeled hexokinase (*24, 28*) at a time of 0 min and 1 mM NaCN was added to the medium after 51 min. At each time point, sets of optical sections were acquired at $z = -1.5, -0.75, -0.25, 0, 0.25, 0.75$, and 1.5 μm centered on a plane of principal interest near the ventral portion of the cell, and each of these sets was restored. (**A**) The central plane in the set 30 min after hexokinase injection and before restoration. (**B** to **F**) The same plane after image restoration at 30, 50, 55, 65, and 80 min after hexokinase injection, respectively. The labeled hexokinase becomes associated with organelles that have been identified as mitochondria, reaching a steady state by 30 min after hexokinase injection. (**G**) The ratio of the fluorescence intensity of localized hexokinase relative to the intensity in a region near the corresponding mitochondrion but not localized (free cytosolic) was computed for the same nine mitochondria in each image and plotted as a function of time after hexokinase injection. Error bars indicate the standard error of the absolute ratio values measured at these nine mitochondria. $\alpha = 0.005$ and 40 iterations were used. In (A) and (B), zero intensity was black and the brightest pixel was white; (C) to (F) were corrected for bleaching and shown with the same scale as (B).

be introduced into a cell must be limited to avoid increasing the number of intracellular copies of that molecule significantly. Images of the distribution of such probes must be obtained with the highest possible collection efficiency and data acquisition speed, a requirement met by the use of standard wide-field optics and high–quantum efficiency, low-noise CCD detectors and by minimization of the number of optical sections (*22*). A few optical sections spaced closely provide high-resolution information in a volume of interest and a few planes spaced farther apart provide information on the origin of out-of-focus light. This information is sufficient for our algorithm to provide accurate high-resolution images from a small number of optical sections (Figs. 1 and 5).

Our method was used in this way to follow the movement of fluorescently tagged hexokinase in response to a metabolic perturbation in a living cell (Fig. 5). In isolated mitochondria, hexokinase binds specifically to sites on the mitochondrial membrane; this binding increases the efficiency of hexokinase and may be regulated by metabolic products (*23*). Rhodamine-X–labeled hexokinase was microinjected into an A7R5 cultured smooth muscle cell. Localization of hexokinase to mitochondria was evident after image restoration (Fig. 5). Rapid release of the fluorescently labeled hexokinase from the mitochondria was evident after inhibition of oxidative metabolism. Dissociation of hexokinase was also detected in response to 2-deoxyglucose (*24*), presumably because it increased the cellular concentration of glucose 6-phosphate, which inhibits hexokinase binding to isolated mitochondria in vitro (*25*). Thus, both cytosolic glucose 6-phosphate and the metabolic state of mitochondria appear to play a role in regulating hexokinase binding to mitochondria in living cells.

There are limitations to our method. The computational time for processing images precludes viewing the restored images in real time, but this time is decreasing as computers become faster. The algorithm has been used on wide-field images of specimens as thick as 350 μm; however, as the thickness increases, the ratio of in-focus to out-of-focus light decreases and degrades the signal-to-noise ratio. Confocal optics or two-photon excitation combined with image restoration would be expected to provide high-resolution views of even the thickest specimens. With our approach, high-resolution three-dimensional views of the local ionic and chemical changes that underlie a wide range of cellular processes can now be studied in both fixed and living cells.

REFERENCES AND NOTES

1. Y. Hiraoka, J. W. Sedat, D. A. Agard, *Science* **238**, 36 (1987); W. A. Carrington, K. E. Fogarty, F. S. Fay, in *The Handbook of Biological Confocal Microscopy*, J. Pawley, Ed. (Plenum, New York, 1989), pp. 151–161.
2. A. Boyde, *Science* **230**, 1270 (1985); G. J. Brakenhoff, H. T. M. van der Voort, E. A. Spronson, W. A. M. Linnemans, N. Nanninga, *Nature* **317**, 748 (1985).
3. W. Denk, J. H. Strickler, W. W. Webb, *Science* **248**, 73 (1990).
4. F. Lanni, B. Bailey, D. L. Farkas, D. L. Taylor, *Bioimaging* **1**, 187 (1993).
5. F. S. Fay, K. E. Fogarty, J. M. Coggins, in *Optical Methods in Cell Physiology*, P. De Weer and B. Salzberg, Eds. (Wiley, New York, 1986), pp. 51–68; F. S. Fay, W. Carrington, K. E. Fogarty, *J. Microsc.* **153**, 133 (1989); W. A. Carrington and K. E. Fogarty, in *Proceedings of the 13th Annual Northeast Bioengineering Conference*, Philadelphia, March, 1987, K. Foster, Ed. (IEEE, New York, 1987), pp. 108–111.
6. D. A. Agard and J. W. Sedat, *Nature* **302**, 676 (1983); D. A. Agard, Y. Hiraoka, J. W. Sedat, P. Shaw, *Methods Cell Biol.* **30**, 353 (1989).
7. V. Krishnamurti, Y.-H. Liu, T. J. Holmes, B. Roysam, J. N. Turner, *SPIE Proc.* **1660**, 95 (1992); J.-A. Conchello, *ibid.* **2302**, 369 (1994).
8. W. A. Carrington, *ibid.* **1205**, 72 (1990).
9. ———, K. E. Fogarty, F. S. Fay, in *Non-Invasive Techniques in Cell Biology*, K. Foster and S. Grinstein, Eds. (Wiley-Liss, New York, 1990), pp. 53–72.
10. K. C. Carter *et al.*, *Science* **259**, 1330 (1993); D. J. Elliot, D. S. Bowman, N. Abovich, F. S. Fay, M. Rosbash, *EMBO J.* **11**, 3731 (1992); F. A. Gonzalez *et al.*, *J. Cell Biol.* **122**, 1089 (1993); K. L. Taneja, L. M. Lifschitz, F. S. Fay, R. H. Singer, *ibid.* **119**, 1245 (1992); M. Joly, A. Kazlauskas, F. S. Fay, S. Corvera, *Science* **263**, 684 (1994).
11. E. D. Moore *et al.*, *Nature* **365**, 657 (1993).
12. A. N. Tikhonov and V. Y. Arsenin, *Solutions of Ill-Posed Problems* (Winston, Washington, DC, 1977); C. W. Groetsch, *The Theory of Tikhonov Regularization for Fredholm Equations of the First Kind*, vol. 105 of *Research Notes in Mathematics* (Pitman, Boston, 1984); R. Coleman, *J. Microsc.* **153**, 233 (1987).
13. W. A. Carrington, thesis, Washington University, MO (1982).
14. J. P. Butler, J. A. Reeds, S. V. Dawson, *SIAM J. Numer. Anal.* **19**, 381 (1982).
15. Finding a continuous function $f(x,y,x) \geq 0$ that minimizes $\Phi(f)$ is a constrained infinite-dimensional optimization problem. $\Phi(f)$ is a continuous, strictly convex function of $L^2(V)$ and thus has a unique minimum on the closed convex set of nonnegative functions in $L^2(V)$. The minimizing nonnegative dye density has the form (*8, 14*) $f(x,y,z) = \max[(0, \sum_{i=1}^{N} c_i k_i(x,y,z)]$, where $c = [c_i]$ is an N dimensional vector that minimizes

$$\psi(c) = \frac{1}{2}\left(\int\int\int_V \{\max[0, \sum_{i=1}^{N} c_i k_i(x,y,z)]\}^2 \, dxdydz + \alpha|c|^2\right) - \sum_{i=1}^{N} c_i \tilde{g}_i$$

This function, $\psi(c)$, is finite dimensional, strictly convex, and twice differentiable; we calculated its gradient and applied a conjugate gradient method to find the unique c that minimizes $\psi(c)$. The fluorescent dye density is then $f(x,y,z) = \max[0, \sum_{i=1}^{N} c_i k_i(x,y,z)]$ for the c that minimizes $\psi(c)$. Because this formulation consistently treats the fluorescent dye density, $f(x,y,z)$, as a function defined on a continuous domain, we have an abstract algorithm for finding the continuous dye density. It has been proven that this approach regularizes this ill-posed problem (*13*). It can also be shown that the numerical algorithm converges from any starting point to the nonnegative minimizer of $\Phi(f)$ in the $L^2(V)$ norm (strong topology). To perform the actual calculations, we must discretize the dye density also, but the grid we choose for discretization can now be finer than the sampling grid. The volume, V, on which $f(x,y,x)$ is calculated can extend beyond the field of view of the camera and beyond the z range of the optical sections acquired. The calculations are normally performed in this manner to obtain estimates of the fluorescent dye density outside the field of view and beyond the z range measured. These extrapolated estimates adequately account for the light that blurs into the image from outside the camera edge, thus eliminating edge artifacts. The point spread function (PSF), $k_i(x,y,z)$, must be known on this discretization grid. In thick living samples, the PSF of an oil immersion lens varies spatially (*18*) [S. Hell, G. Reiner, C. Cremer, E. H. K. Stelzer, *J. Microsc.* **169**, 391 (1993)], which can be treated by allowing each $k_i(x,y,z)$ to be different. Alternatively, a water immersion lens has an invariant PSF and less aberration [P. K. Gasbjerg *et al.*, *Biophys. J.* **66**, A274 (abstr.) (1994); M. Brenner, *Am. Lab.* **26**, 14 (1994)]. Other image restoration methods that incorporate nonnegativity and a form of smoothing term include maximum entropy [S. F. Gull and G. J. Daniell, *Nature* **272**, 686 (1978)], projection onto convex sets (POCS) [M. Koshy, D. A. Agard, J. W. Sedat, *SPIE Proc.* **1205**, 64 (1990)], and Bayesian methods [K. Hanson, in *Image Recovery: Theory and Applications*, H. Stark, Ed. (Academic Press, New York, 1987), pp. 79–127]. Our approach differs from these others in explicitly considering the data as discrete and the cell as a continuous object, in the consistent use of this formulation in the numerical implementation of the algorithm, and in its robust and rapid convergence to that continuous object in the strong topology. These other methods have so far had limited success in applications to fluorescence microscopy. Other methods that incorporate nonnegativity and that are routinely applied to fluorescence microscopy (*6, 7*) have not been used to restore on a finer grid than the data and require more data, and thus more light exposure, than our approach.
16. The cone of missing frequencies was recovered in all the restored images. Defining the spatial frequency cutoff in x or z to be the highest spatial frequency, k_x or k_z, where the magnitude is >1% of the DC (zero frequency) magnitude, we showed that for the data in Fig. 1, k_x = 1/210 nm and k_z = 1/533 nm, and restored k_x = 1/50 nm and k_z = 1/100 nm; for the data in Fig. 3 (calculated from PSF), k_x = 1/289 nm and k_z = 1/1200 nm, and restored k_x = 1/56 nm and k_z = 1/100 nm; for the data in Fig. 4 (calculated from PSF), k_x = 1/357 nm and k_z = 1/1285 nm, restored (not subpixel) k_x = 1/208 nm and k_z = 1/582 nm, and restored (subpixel) k_x = 1/93 nm and k_z = 1/437 nm; and for the data in Fig. 5, k_x = 1/1898 nm and restored k_x = 1/1097 nm (because the data in Fig. 5 are not regularly spaced, k_z was not calculated).
17. L. L. Tella, thesis, Worcester Polytechnic Institute (1985).
18. S. Frisken-Gibson and F. Lanni, *J. Opt. Soc. Am. A* **6**, 9 (1989).
19. M. Iino, *Biochem. Biophys. Res. Commun.* **42**, 47 (1987).
20. A. Guerrero, M. T. Kirber, J. J. Singer, F. S. Fay, *Biophys. J.* **64**, A153 (abstr.) (1993).
21. L. M. Loew, W. A. Carrington, R. A. Tuft, F. S. Fay, *Proc. Natl. Acad. Sci. U.S.A.* **91**, 12579 (1994); L. M. Loew, R. A. Tuft; W. A. Carrington, F. S. Fay, *Biophys. J.* **65**, 2396 (1993).
22. R. A. Tuft, D. S. Bowman, W. Carrington, F. S. Fay, *Biophys. J.* **61**, A34 (abstr.) (1992).
23. J. E. Wilson, in *Microcompartmentation*, D. P. Jones, Ed. (CRC Press, Boca Raton, FL, 1988), pp. 172–188.
24. R. M. Lynch, K. E. Fogarty, W. Carrington, F. S. Fay, *Biophys. J.* **59**, A157 (abstr.) (1991).
25. J. E. Wilson, *Curr. Top. Cell Regul.* **16**, 1 (1980).
26. The PSF is band-limited and so convolving with the cylindrical band-limit function, BL, leaves the result unchanged, which has the effect of imposing a band-limit constraint. Because the bead image is (PSF*PIXEL)*(BEAD*BL) and because both BEAD

and BL can be calculated to any pixel size, we can apply our subpixel algorithm to the bead image using for a PSF, BEAD*BL. The result is then PSF*PIXEL calculated with finer sampling than the original pixel size and with the elimination of error because of the use of a large bead instead of a point source. α = 0.005 and 15 iterations were used. The beads used are manufactured (Molecular Probes) with the dye distributed uniformly throughout their volume.

27. NRK1 cells were fixed and then prepared for immunocytochemistry; microtubules were stained with mouse monoclonal antibodies to β-tubulin (Amersham) and rhodamine-labeled goat antibodies to mouse immunoglobulin (TAGO).
28. The cell was injected with rhodamine-X–labeled hexokinase (dye:protein, ~0.8), which exhibited normal activity, to a final concentration of 0.09 mg/ml at 0 min.
29. We thank D. Fishkein for NRK-1 cells labeled with antibodies to tubulin, D. Bowman and R. Tuft for hardware development, and J. Carmichael for photographic assistance. Supported by grants from NSF (W.A.C., F.S.F.); NIH (W.A.C., F.S.F., R.M.L.); American Heart Association, Massachusetts affiliate (E.D.W.M.); Medical Foundation of Boston (R.M.L.); North Atlantic Treaty Organization (G.I., F.S.F.); and American Diabetes Association (R.M.L.).

5 October 1994; accepted 6 March 1995

Repositioning of a Domain in a Modular Polyketide Synthase to Promote Specific Chain Cleavage

Jesus Cortes, Kirsten E. H. Wiesmann, Gareth A. Roberts,* Murray J. B. Brown, James Staunton, Peter F. Leadlay†

Macrocyclic polyketides exhibit an impressive range of medically useful activities, and there is great interest in manipulating the genes that govern their synthesis. The 6-deoxyerythronolide B synthase (DEBS) of *Saccharopolyspora erythraea*, which synthesizes the aglycone core of the antibiotic erythromycin A, has been modified by repositioning of a chain-terminating cyclase domain to the carboxyl-terminus of DEBS1, the multienzyme that catalyzes the first two rounds of polyketide chain extension. The resulting mutant markedly accelerates formation of the predicted triketide lactone, compared to a control in which the repositioned domain is inactive. Repositioning of the cyclase should be generally useful for redirecting polyketide synthesis to obtain polyketides of specified chain lengths.

Complex polyketides are natural products, found predominantly in *Streptomyces* and related filamentous bacteria, that exhibit an impressive range of antibiotic, anticancer, antiparasite, and immunosuppressant activities. Despite their apparent structural diversity, they are synthesized by a common pathway in which units derived from acetate or propionate are condensed onto the growing chain, in a process resembling fatty acid biosynthesis (*1*). The intermediates remain bound to the polyketide synthase (PKS) during multiple cycles of chain extension and (to variable extent) reduction of the β-keto group formed in each condensation (Fig. 1). The structural variation between naturally occurring polyketides arises largely from the way each PKS controls the number and type of units added, and the extent and stereochemistry of reduction at each cycle. In addition, the product of the PKS is frequently acted upon by regiospecific glycosylases, methyltransferases, and oxidative enzymes, to produce still greater diversity.

Sequencing of the structural genes for PKSs has revealed fundamental differences in the organization of the synthases producing aromatic polyketides and complex, reduced polyketides. For aromatic polyketides, the PKS consists of a single set of enzyme activities (*2*), housed either in a single polypeptide chain (type I) or on separate polypeptides (type II), that act in every cycle. In contrast, complex polyketides are synthesized on multifunctional PKSs that contain a distinct active site for every catalyzed step in chain synthesis (*3*–*5*). For example, the clinically important antibiotic erythromycin A is derived from propionyl–coenzyme A (propionyl-CoA) and six molecules of (2*S*)-methylmalonyl-CoA (*6*) through the sequential action of six such sets of enzymes housed in the three multienzyme polypeptides (*7*) of 6-deoxyerythronolide B synthase (DEBS) (Fig. 1).

The discovery of the organization of such "modular" PKSs has prompted attempts, with mixed success, to delete the active sites of individual domains in order to produce an altered product of predicted structure. Deletion of the entire ketoreductase (KR) domain from cycle 5 of DEBS (*4*) and mutation of active site residues in the enoylreductase (ER) active site from cycle 4

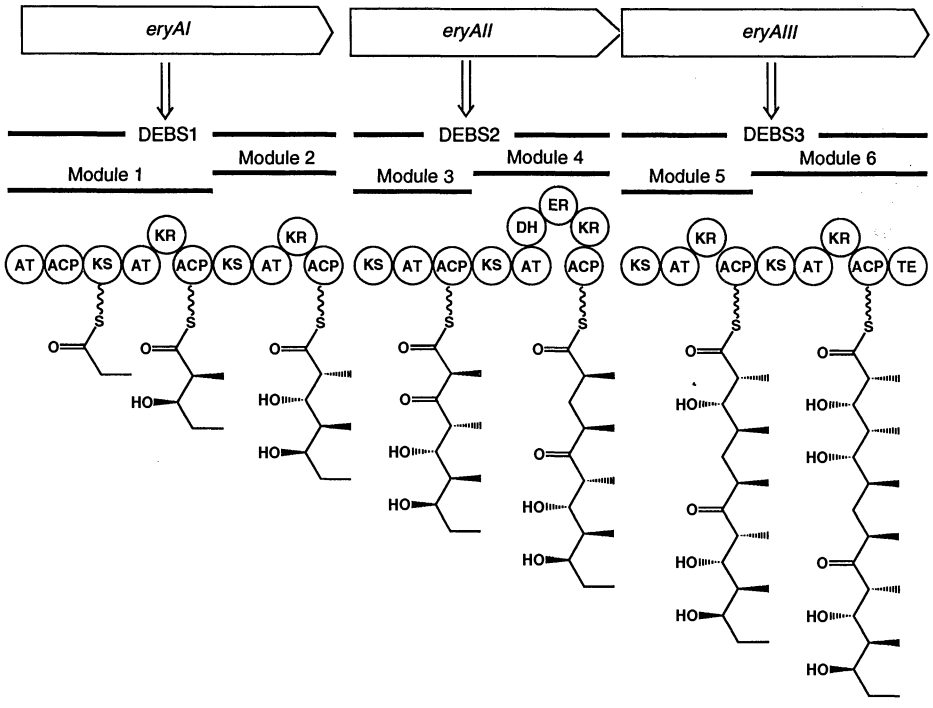

Fig. 1. The domain organization of 6-deoxyerythronolide B synthase (DEBS) [adapted from (*9*) with permission]. Each protein module contains an acyl carrier protein (ACP), an acyltransferase (AT), and a β-ketoacyl-ACP synthase (KS), and some modules also contain activities for reduction [β-ketoacyl-ACP reductase (KR), dehydratase (DH), and enoyl reductase (ER)]. In the mutants described in this report, the thioesterase-cyclase (TE) at the end of module 6, which normally cyclizes the full-length chain to 6-deoxyerythronolide B, is fused to the COOH-terminus of DEBS1.